metals

MDPI

Article

Optimization of Multi-Pass Cold Drawing and Annealing for High-Purity Vanadium Wires

Yanhui Wang [1,2,3], Shilong Pan [2,3], Xuewei Lv [1,*], Rui Tang [2,3], Qi Liu [2,3], Anzhong Zhao [4], Xinwei Bo [2,3] and Yilong Zhong [2,3]

[1] College of Materials Science and Engineering, Chongqing University, Chongqing 400044, China; woshiamong@126.com
[2] Chongqing Material Research Institute Co., Ltd., Chongqing 400707, China; panshilong1999@163.com (S.P.); ruitang_cq@163.com (R.T.); liuqi@cmri.cc (Q.L.); boxinwei@cmri.cc (X.B.); ylzhong_999@163.com (Y.Z.)
[3] National Engineering Research Center for Instrument Function Materials, Chongqing 400707, China
[4] Sinomach Academy of Science and Technology Co., Ltd., Beijing 100050, China; ncfma06@126.com
* Correspondence: lvxuewei@163.com

Abstract

Multi-pass cold drawing and subsequent annealing are critical processing steps determining the microstructure and mechanical performance of vanadium wires, as they directly influence the performance of the final product. This study systematically investigated the microstructural evolution and mechanical property changes of high-purity vanadium wire during multi-pass cold drawing and annealing, which was prepared by combining powder metallurgy and electron beam melting, with the aim of establishing an optimal processing window for nuclear-grade applications. The results indicated that cold drawing progressively transformed the equiaxed grains into a fibrous microstructure, accompanied by pronounced work hardening dominated by dislocation accumulation. At a strain of 0.71, the tensile strength increased to 467 MPa, while elongation decreased to 2.3%, with dislocation strengthening contributing to over 50% of the strength increment. Annealing processed through three distinct stages: recovery (600–700 °C), recrystallization (800–900 °C), and rapid grain growth (1000 °C). Complete recrystallization eliminated the cold-worked substructure, resulting in the loss of work hardening and a tensile strength below the nuclear-grade requirement. The optimal processing route involved high-strain cold drawing followed by recovery annealing at 600–700 °C, resulting in wires with a tensile strength greater than 430 MPa and elongation exceeding 14%, thereby fully meeting the specifications for self-powered neutron detectors. This work provides practical guidance for the industrial production of vanadium wires for self-powered neutron detector.

Keywords: vanadium wires; multi-pass cold drawing; annealing; self-powered neutron detector; microstructure; mechanical properties

Check for updates

Academic Editors: Young-Min Kim, Minjung Kang and Duck Bong Kim

Received: 12 September 2026
Revised: 4 October 2026
Accepted: 9 October 2026
Published: 15 October 2026

Copyright: © 2026 by the authors. Licensee MDPI, Basel, Switzerland. This article is an open access article distributed under the terms and conditions of the Creative Commons Attribution (CC BY) license.

1. Introduction

Vanadium self-powered neutron detectors (VSPND) are widely used for in-core neutron flux monitoring in AP1000 and CAP1400 reactor cores owing to their high reliability, simple structure, and long service life. It enables precise measurement of neutron population dynamics, quantitative assessment of power density distribution, and significant enhancement of both operational safety and efficiency of the reactor [1,2]. As the core sensing element of VSPND, the vanadium wire must meet stringent requirements in terms of dimensions, metallurgical purity, and mechanical properties. Typically, vanadium

wire has a purity of no less than 99.90% and a diameter ranging from 1.0 ± 0.01 mm to 1.5 ± 0.01 mm; these parameters are closely related to signal sensitivity. Importantly, the wire must exhibit a tensile strength greater than 400 MPa and an elongation exceeding 8%, as these mechanical characteristics directly influence the reliability and service life of the detector [3].

To date, studies focusing specifically on vanadium wire remain scarce. Most research has been directed toward the irradiation damage, hydrogen embrittlement, and high-temperature properties of vanadium and its alloys (e.g., V-Cr-Ti), which are largely unrelated to the manufacturing process of vanadium wire [4,5]. Some investigations have indicated that severe plastic deformation (SPD) techniques, such as equal-channel angular pressing (ECAP) [6,7] and high-pressure torsion (HPT) [8,9], have been widely employed to produce ultrafine-grained or nanocrystalline vanadium, thereby significantly enhancing its strength. Nevertheless, the application of these SPD methods to the continuous, industrial scale production of vanadium wire still presents considerable challenges in terms of dimensional control and production efficiency. Therefore, optimizing the processing route to simultaneously satisfy these mechanical requirements remains a prerequisite for manufacturing vanadium wires.

The industrial production of high-purity vanadium wires typically involves multiple processes, including smelting, plastic forming, and heat treatment [10]. Among these processes, multi-pass drawing is a critical forming step for achieving precise dimensions and target microstructures [11]. As a typical body-centered cubic (BCC) metal, vanadium undergoes slip-dominated plastic deformation under conventional processing conditions, with deformation twinning becoming active only at cryogenic temperatures (e.g., −196 °C) [12–14]. The predominant slip system in BCC metals is {110} <111>, which typically leads to the formation of a strong <110> fiber texture during wire drawing [15,16]. Cold drawing promotes dislocation accumulation, which enhances strength through dislocation interactions and grain boundary effects, but simultaneously induces severe work hardening and a loss of ductility. Subsequent annealing can restore ductility via recovery and recrystallization, albeit at the expense of a significant reduction in strength. This strength–ductility trade-off constitutes the fundamental material challenge in fabricating vanadium wire that meets nuclear-grade specifications [17–21]. Currently, there is a lack of mechanistic studies and established process design windows for the synergistic optimization of strength and ductility in vanadium wire during multi-pass cold drawing and annealing. Consequently, the strengthening mechanisms operative during cold drawing, as well as the microstructural and property evolution following annealing, still require systematic investigation.

Despite its industrial importance, the relationships among drawing strain, microstructural evolution, strengthening mechanisms, and post-annealing mechanical properties of high-purity vanadium wires remain poorly understood. This study aims to elucidate the regulatory effects of multi-pass cold drawing and subsequent vacuum annealing on the microstructure and mechanical properties of high-purity vanadium wires, to address the strength–ductility trade-off challenge in the fabrication of vanadium wires, and to propose a processing strategy for optimizing the mechanical performance of high-purity vanadium wires.

2. Materials and Experimental Methods

2.1. Materials and Processing Route

The raw material used in this study was high-purity vanadium powder (99.95% purity). The vanadium powder was compacted by cold isostatic pressing to form billets with uniform distribution and adequate density. These billets were pre-sintered under vacuum

to enhance density and reduce gaseous impurities, followed by double remelting in an electron beam melting furnace (Guilin Shida Technology Co., Ltd., Guilin, China). The remelted billets were vacuum-annealed at 900–1000 °C, yielding a final vanadium ingot weighing 3 kg. A high-temperature oxidation-resistant silicon coating was applied to the surface of the vanadium ingot to minimize atmospheric contamination during thermal processing. The vanadium ingot was subjected to repeated hot forging at 700–1000 °C until reduced to a rod of approximately 15 mm in diameter, achieving a total deformation of 85%. The rod was then vacuum annealed at 900 °C. Subsequently, multi-pass cold drawing converted the rod into wires with diameters of 2.0 mm, 1.9 mm, 1.8 mm, 1.7 mm, 1.6 mm, 1.5 mm and 1.4 mm (Figure 1a), followed by surface pickling for 3 min in an aqueous solution containing 5% HF and 5% HNO_3. The macro-morphology of the vanadium samples at different processing stages is shown in Figure S1. The 1.4 mm diameter wires were annealed in vacuum at temperatures of 600 °C, 700 °C, 800 °C, 900 °C and 1000 °C for 30 min each. The true strain of wires was calculated using the following formula:

$$\varepsilon = ln\left(\frac{{d_0}^2}{{d_i}^2}\right) \quad (1)$$

where d_0 is the diameter before drawing and d_i is the diameter after drawing. The 2.00 mm wire after sufficient annealing was used as the wire with zero strain.

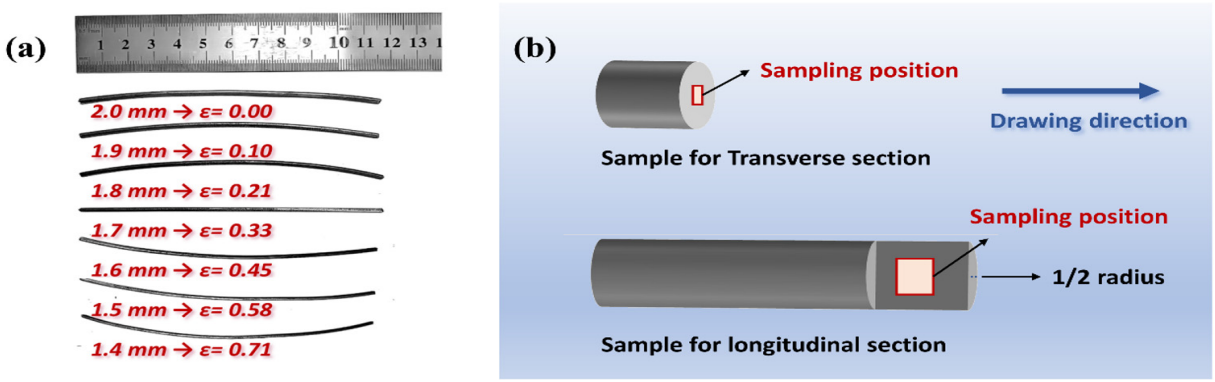


Figure 1. (**a**) Photographs of vanadium wires with different diameters. (**b**) Schematic illustration of sampling locations for microstructural observation.

The selected drawing strains (ε up to 0.71) and annealing temperatures (600–1000 °C) were designed to systematically span the entire range from work-hardened state to full recrystallization and subsequent grain coarsening, enabling identification of an optimal process window for vanadium wires.

2.2. Microstructure Characterization

Tensile testing of the vanadium wires was conducted using a Shimadzu AGS-X electronic universal testing machine (Shimadzu Corporation, Kyoto, Japan); the gauge length was 50 mm, the speed was 5 mm/min, and three specimens were tested for each condition to ensure the accuracy of the results. Microhardness was measured at both the edge and core regions using an Innovatest Falcon 500 Vickers hardness tester (Innovatest Europe B.V., Maastricht, The Netherlands) under a load of 200 gf for a dwell time of 10 s, with at least three measurements performed in each region. Chemical composition analysis was performed using an Agilent 5800 inductively coupled plasma optical emission spectrometer (ICP-OES) (Agilent Technologies, Inc., Santa Clara, CA, USA), and the results are presented in Table 1. For electron backscatter diffraction (EBSD) characterization, wire specimens were

sectioned as illustrated in Figure 1b, hot-mounted in resin, and then sequentially ground, mechanically polished, and electropolished in a solution containing 20% H_2SO_4 and 80% CH_3OH (v/v) at 20 V for 20 s. EBSD data were acquired using a Zeiss Sigma field-emission scanning electron microscope (SEM) (Carl Zeiss AG, Oberkochen, Germany) equipped with an Oxford Nordlys Max EBSD detector (Oxford Instruments, High Wycombe, UK) at a step size of 0.6 μm and an accelerating voltage of 20 kV. For each measurement region, an area of approximately 0.5 mm × 0.5 mm was scanned. Given the wire diameters of 2.0–1.4 mm, this scanned area is sufficiently large to contain a statistically meaningful number of grains for reliable microstructural analysis. The acquired EBSD data were processed and analyzed using AZtecCrystal software (Version 2.1). Low-angle grain boundaries (LAGBs) and high-angle grain boundaries (HAGBs) were defined as boundaries with misorientation angles of $2^\circ < \theta < 10^\circ$ and $\theta > 10^\circ$, respectively. Recrystallized, substructured, and deformed grains were identified based on the grain orientation spread (GOS); grains with GOS $\leq 2^\circ$ were considered recrystallized. The kernel average misorientation (KAM) was calculated using a 3 × 3 kernel with a maximum misorientation threshold of 5°. The geometrically necessary dislocation (GND) density was estimated from the average KAM using $\rho^{GND} = 2KAM/(\mu b)$, where b = 0.26 nm is the Burgers vector of BCC vanadium and x is the EBSD step size.

Table 1. Chemical composition of vanadium wire (wt.%).

Element	V	B	Cd	Fe	Ni	Mn	Co	Al
Content	Bal.	<0.0005	<0.0005	<0.001	0.001	<0.0005	<0.0005	0.0008
Element	Mg	Cu	Cr	K	Sb	Na	Pb	Si
Content	0.0003	<0.0005	<0.0002	0.0005	<0.0005	<0.001	<0.0005	<0.0001

3. Results

3.1. Cold Drawing of Vanadium Wires

3.1.1. Microstructure at Different Drawing Strains

Surface morphology evolution closely correlates with the near-surface plastic deformation and work-hardening behavior during cold drawing. Surface morphologies of the vanadium wires after multi-pass cold drawing are shown in Figure 2. All samples were directly pickled after cold drawing. With increasing strain, distinct features induced by plastic deformation became evident on the wire surface. Parallel grooves oriented along the drawing direction were observed, which are attributed to friction between the wire and the drawing die. Moreover, as a result of work-hardening-induced surface embrittlement, characteristic flake-like spalling pits, approximately 10–15 μm in diameter, formed on the surface Figure 2c.

The evolution of grain morphology, orientation and size during cold drawing is the fundamental for understanding the plastic deformation mechanism and work-hardening behavior of BCC metals. To directly capture the grain elongation and orientation rotation along the deformation axis, EBSD characterization was performed on longitudinal sections parallel to the drawing direction (DD) for all samples. Figure 3 illustrates the inverse pole figure (IPF) maps and the corresponding average grain size evolution of vanadium wires subjected to different strains. As shown in Figure 3a, the initial vanadium wire ($\varepsilon = 0$) exhibited a strong preferred orientation, dominated by a <110>//drawing direction (DD) texture component. This textural characteristic is likely inherited from the orientation inheritance during the prior recrystallization process, where the nucleation and growth of new grains are preferentially governed by the pre-existing deformation substructure. At this stage, the grains presented a nearly equiaxed morphology with an average size of

10.6 μm (Figure 3d). With increasing drawing strain, the original equiaxed grains were progressively elongated along the DD, gradually forming a typical fibrous microstructure. Concurrently, the texture evolved continuously: the fraction of the <110> component decreased, while the <100> component was gradually strengthened, indicating significant crystal rotation induced by plastic deformation. Meanwhile, the original grains were continuously subdivided into finer subgrains and grains, leading to overall grain refinement. At a true strain of 0.71 (Figure 3f), the volume fraction of fine grains (≤5 μm) increased sharply to 56.5%, and the average grain size decreased to 7.5 μm, confirming the grain refinement effect induced by cold drawing.

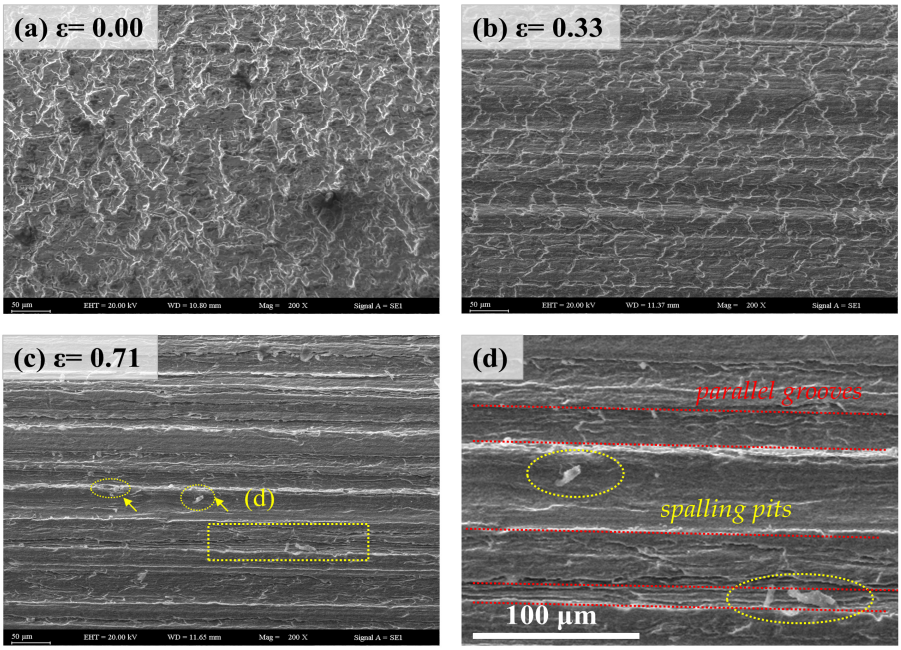


Figure 2. Surface morphology of the vanadium wire after cold drawing at different strains: (**a**) ε = 0; (**b**) ε = 0.33; (**c**) ε = 0.71; (**d**) magnified view of (**c**).

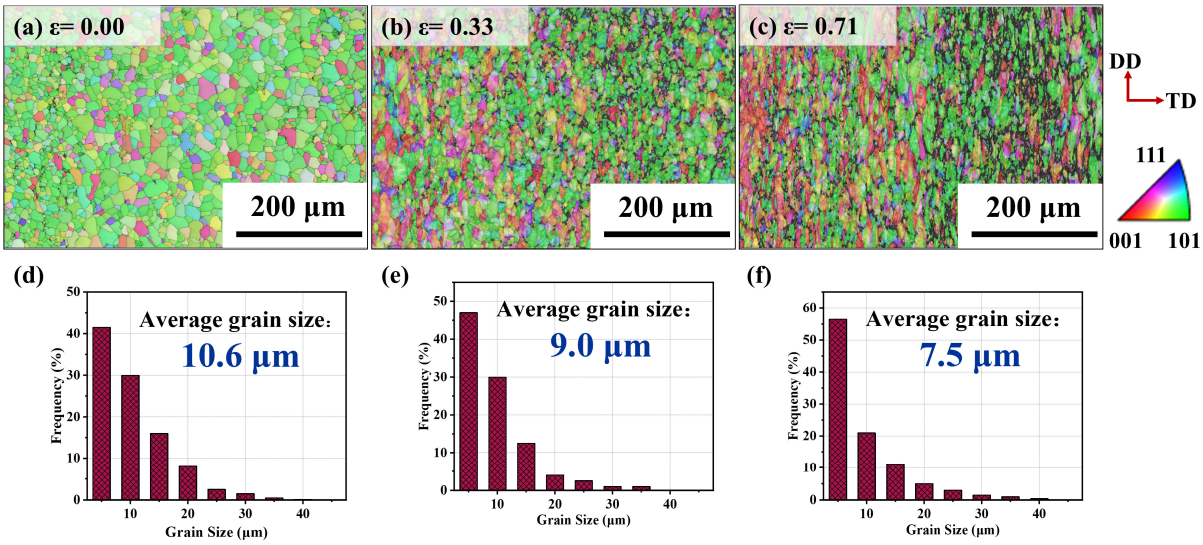


Figure 3. (**a**–**c**) IPF maps and (**d**–**f**) grain size distribution maps of the vanadium wires at different strains: (**a**,**d**) ε = 0; (**b**,**e**) ε = 0.33; (**c**,**f**) ε = 0.71. The color code and reference direction for the IPF maps are provided.

In metallic materials, the evolution of grain boundary character distribution during plastic deformation exerts a profound influence on their mechanical properties. For instance, HAGBs generally act as effective barriers to dislocation motion, thereby contributing to the strengthening and hardening of metallic materials [22]. In contrast, LAGBs, which are composed of ordered arrays of dislocations, offer lower resistance to dislocation glide and can be penetrated by mobile dislocations [23,24]. Figure 4 presents the evolution of GBCD in vanadium wires as a function of cold drawing true strain. As the strain increased from 0 to 0.33, the fraction of HAGBs decreased sharply from 92.4% to 35.3%, while the fraction of LAGBs increased concomitantly. This rapid transformation suggests that extensive dislocation multiplication and rearrangement occur at low-to-medium strains, leading to the formation of dense dislocation walls and nascent subgrain boundaries within the original grains [25]. However, the rate of this transformation decelerated significantly when the strain exceeded 0.33. At $\varepsilon = 0.71$, the HAGB fraction reached a plateau at approximately 18.4%, suggesting that the subgrain structure attained a quasi-steady state under the given deformation conditions. This is further corroborated by the KAM distributions and the evolution of GND density, as shown in Figure 5. In the initial state, the KAM map predominantly exhibited blue regions corresponding to low misorientation, with only sporadic green regions of intermediate misorientation, indicative of a relatively low residual stress level. As the strain increased, green-to-yellow regions representing medium-to-high local misorientation expanded markedly. Concurrently, the GND density exhibited a continuous increasing trend with strain, rising from 0.81×10^{14} m^{-2} in the initial state to 4.68×10^{14} m^{-2} at a strain of 0.71. Notably, the GND density tended to stabilize when the true strain reached 0.58.

Figure 6 presents the pole figures and inverse pole figures of high-purity vanadium wires at different drawing strains. The <110>//DD fiber texture remained dominant throughout all processing stages. In the initial state (Figure 6a), a strong <110> orientation was evident from the high pole density along the drawing direction and the sharp peak in the inverse pole figure. As the strain increased, the texture composition evolved, marked by the appearance of a <100> component along the transverse direction (TD) (Figure 6b), indicating crystal reorientation. At $\varepsilon = 0.71$ (Figure 6c), the <100>//TD component intensified considerably. A steady decrease in the maximum pole density was also observed. This indicates that although the <110>//DD fiber texture remains dominant throughout deformation, its degree of preferred orientation gradually weakens with increasing strain, and the crystal orientation distribution becomes more scattered, revealing a texture weakening effect caused by the combined action of dynamic recovery and grain rotation during plastic deformation.

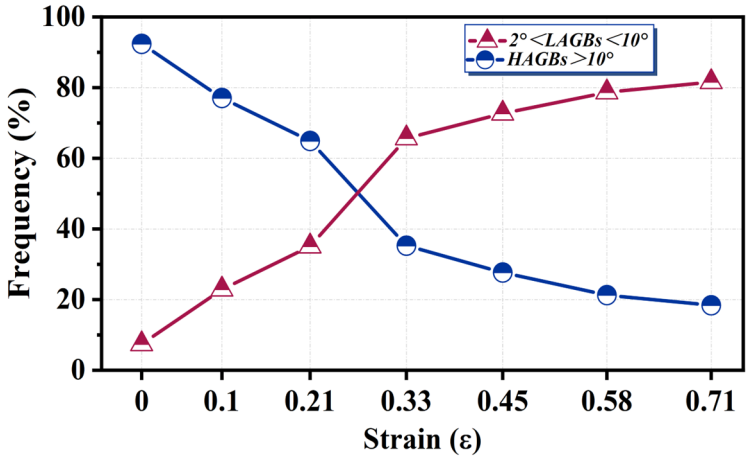


Figure 4. Evolution of LAGB and HAGB fractions with strain.

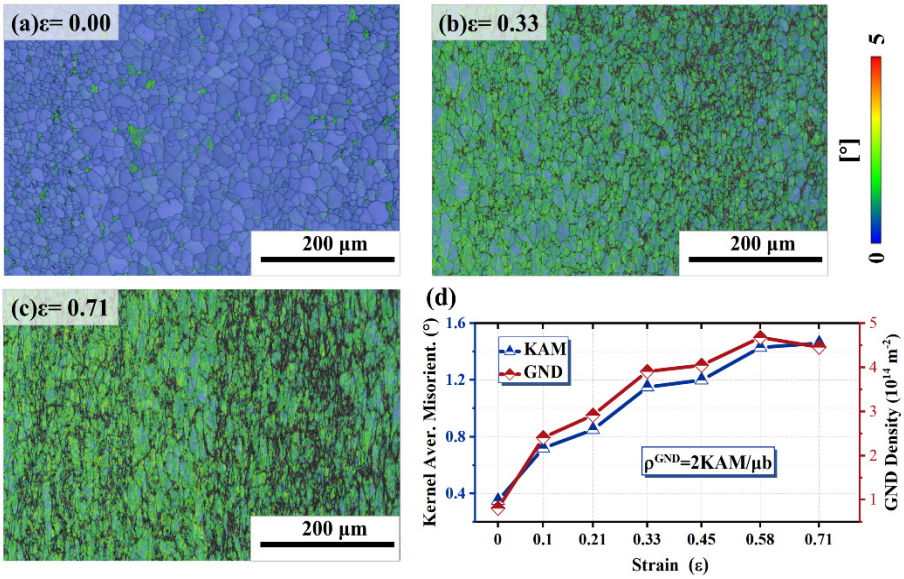


Figure 5. (**a**–**c**) KAM maps of vanadium wires at different strains; (**d**) KAM value and GND density as functions of strain.

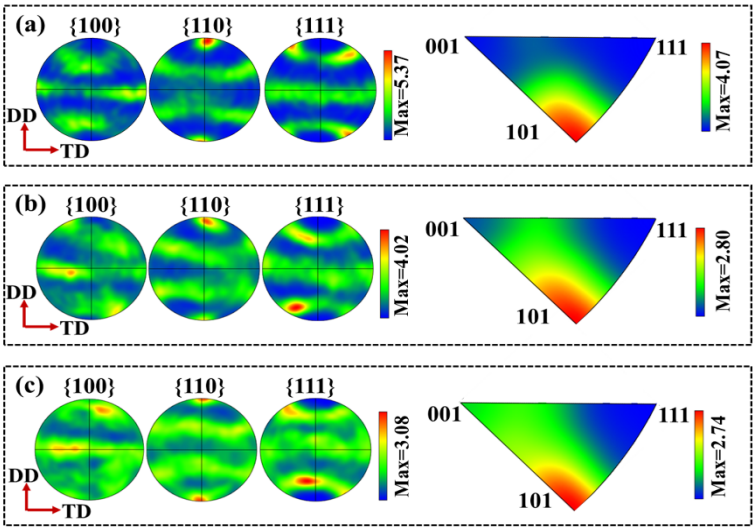


Figure 6. Pole figures and inverse pole figures of the vanadium wires at different strains: (**a**) ε = 0; (**b**) ε = 0.33; (**c**) ε = 0.71.

3.1.2. Mechanical Properties at Different Drawing Strains

Uniaxial tensile tests were conducted at room temperature on vanadium wires processed with different cold drawing strains. Figure 7 presents the engineering stress–strain curves and the evolution of key mechanical properties for each sample. The detailed tensile curves for each condition are provided in Supplementary Figure S2. As vanadium is a ductile metal at room temperature, all specimens exhibited significant necking, consistent with the previously reported literature [7]. The initial vanadium wire had a tensile strength of 328 MPa and an elongation of 30.8%. After straining to ε = 0.1, the tensile strength increased significantly to 400 MPa, while the elongation decreased markedly to 7.7%, indicating pronounced plastic exhaustion. This abrupt loss in ductility was attributed to the rapid multiplication of dislocations and the impediment of their glide, as evidenced by the increase in KAM value (Figure 5). With further increase in strain, the strength continued to rise while the elongation gradually decreased, demonstrating typical work-hardening behavior. At ε = 0.71, the tensile strength reached 467 MPa with an elongation of 2.3%.

Overall, cold working significantly enhanced the strength of the wires, resulting in an approximately twofold increase in yield strength (from 208 MPa in the initial state to 429 MPa).

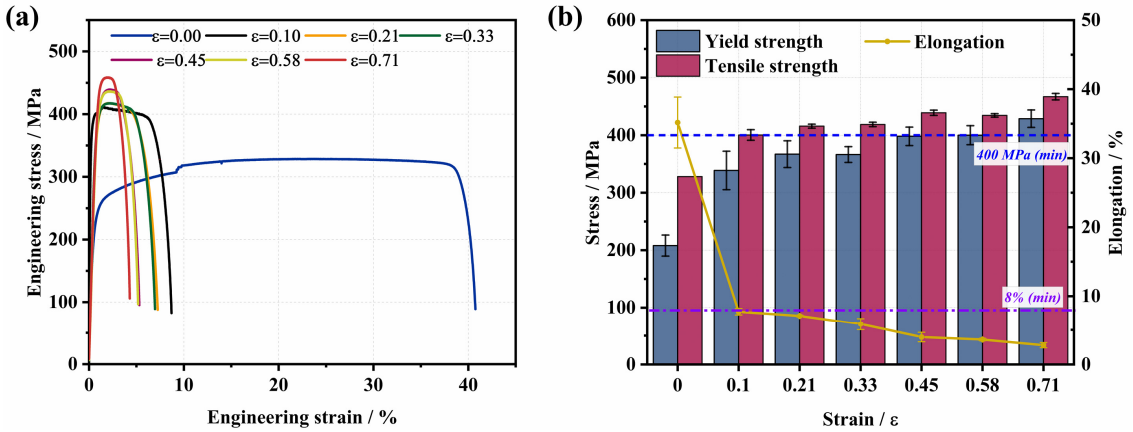


Figure 7. (**a**) Engineering stress–strain curves of vanadium wires at different drawing strains. (**b**) Tensile strength, yield strength, and elongation as functions of drawing strain. Each data point represents the average of at least three independent measurements under the same condition, and the error bars denote one standard deviation. The blue and purple dashed lines indicate the required minimum tensile strength (400 MPa) and elongation (8%), respectively.

Figure 8 shows the microhardness at the peripheral and core regions of the vanadium wires after different drawing strains. The core region was defined as the center of the wire cross-section, while the peripheral region referred to the area within 0.1 mm of the outer surface. The results show that as the strain increased, the microhardness at the periphery and core increased from 136 $HV_{0.2}$ and 119 $HV_{0.2}$ in the initial state to 235 $HV_{0.2}$ and 135 $HV_{0.2}$ at $\varepsilon = 0.71$, respectively. The hardness at the periphery consistently exceeded that at the core. This discrepancy was attributed to the complex stress state experienced by the wire during drawing, which resulted in heterogeneous plastic deformation across the cross-section. The surface region was subjected to high shear stresses and frictional forces in addition to tensile stress, introducing a substantial shear strain component superimposed on the axial deformation. In contrast, the core region experienced primarily uniaxial tensile stress with negligible additional strain components [26,27].

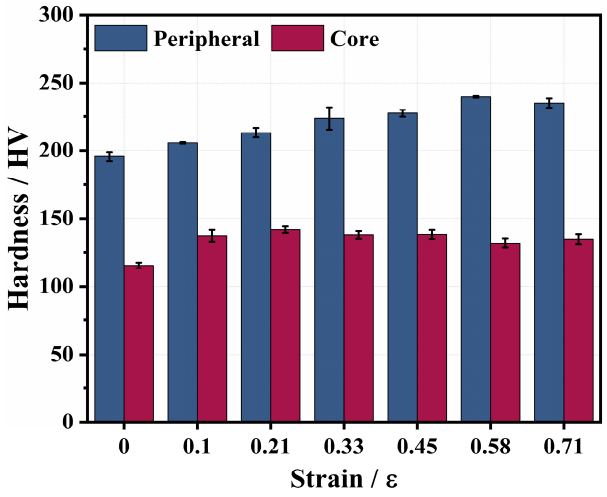


Figure 8. The microhardness at the peripheral and core regions of the vanadium wires at different tensile strains. Each data point represents the average of at least three independent measurements under the same condition, and the error bars denote one standard deviation.

3.2. Annealing of Vanadium Wires

3.2.1. Microstructure at Different Annealing Temperatures

To investigate the influence of annealing temperature on the microstructure evolution of cold-drawn vanadium wires, the IPF maps and corresponding grain size statistics at different annealing temperatures are presented in Figure 9. After annealing at 600 °C, the grain orientation remained dominated by the <100> and <110> textures inherited from the as-drawn condition, accompanied by a weak <111> component. The average grain size was 10.0 μm, exhibiting a slight increase relative to the as-drawn state. At 700 °C, the grain size increased to 12.8 μm. The microstructure at this temperature was still characterized by deformed fibrous structures, indicating that no significant recrystallization had occurred. When the annealing temperature reached 800 °C, the microstructure transformed from a fibrous morphology to equiaxed recrystallized grains. As the temperature further increased to 1000 °C, the grain size increased dramatically to 120.4 μm, approximately five times that after annealing at 900 °C, demonstrating significant grain growth behavior driven by high-temperature atomic diffusion. Meanwhile, the <111> orientation component almost completely disappeared, which is attributed to the preferential growth of grains with <110> and <100> orientations during high-temperature annealing.

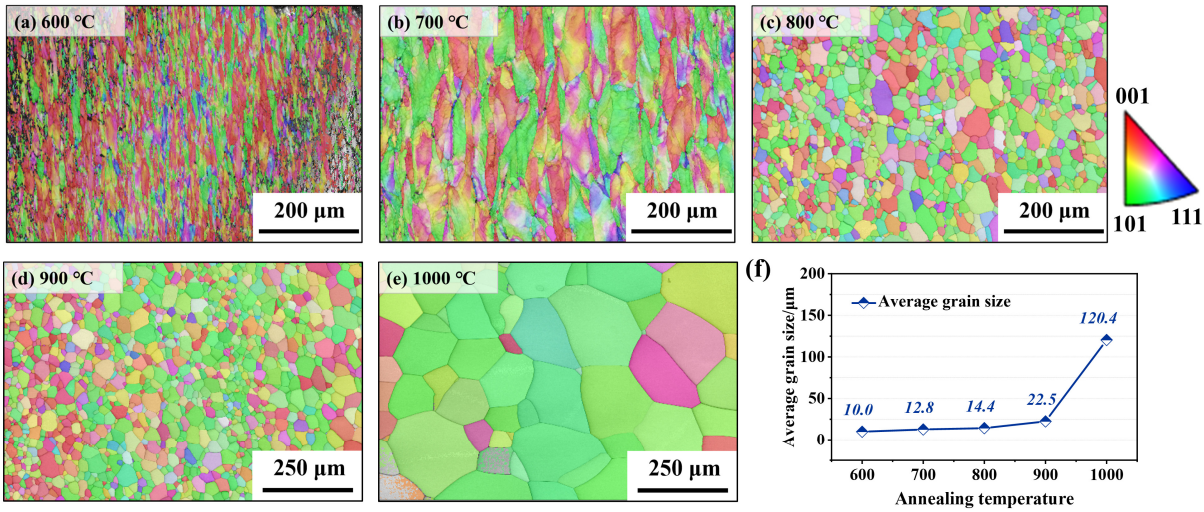


Figure 9. (**a**–**e**) IPF maps and (**f**) grain size distributions of vanadium wires after annealing at different temperatures: (**a**) 600 °C; (**b**) 700 °C; (**c**) 800 °C; (**d**) 900 °C; (**e**) 1000 °C.

As shown in Figure 10, the fractions of LAGBs were 77.0% and 68.1% after annealing at 600 °C and 700 °C, respectively. These results indicate that a high density of dislocation substructures was retained in the material, with most of the stored deformation energy remaining unreleased. The GOS distributions (Figure 11) further confirm the absence of substantial recrystallization at these temperatures. When the annealing temperature was increased to 800 °C, the fraction of HAGBs increased sharply to 95.5%. Concurrently, the fraction of grains with low GOS values (≤2°) increased significantly (Figure 11c), and the microstructure transformed into a predominantly equiaxed grain morphology. These results suggest that 800 °C is the critical temperature for the completion of recrystallization in the vanadium wires.

The characterization of annealing texture evolution is critical for understanding the recrystallization behavior of vanadium wires. After annealing at 600 °C, the texture was dominated by the <100> orientation, as shown in Figure 12. As the temperature increased to 700 °C, the predominant texture shifted from <100> to <110>//DD. Concurrently, the radial <100> component disappeared completely with increasing temperature. After

annealing at 1000 °C, the <110>//DD texture was further strengthened. This may be attributed to the preferential growth of <110>-oriented recrystallized grains. On the one hand, the <110> orientation possesses relatively high stored energy, which provides a larger driving force for recrystallization nucleation and growth; on the other hand, the <110> rotation axis is generally considered to exhibit the fastest grain boundary mobility at a given misorientation [28]. In general, orientations with higher stored energy are more prone to preferential recrystallization nucleation and growth [29]. Such orientation-dependent recrystallization behavior has been reported in high-purity vanadium and BCC metals [30].

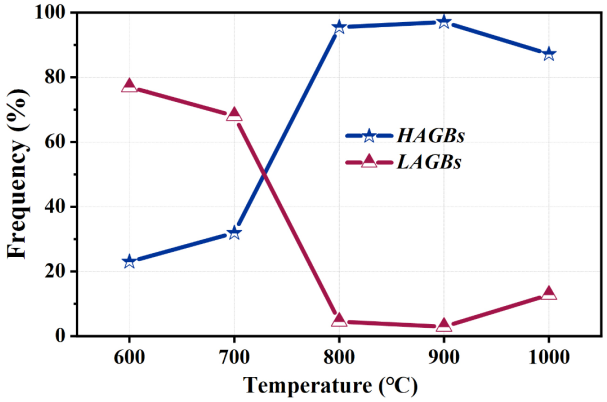


Figure 10. Evolution of LAGB and HAGB fractions with annealing temperatures.

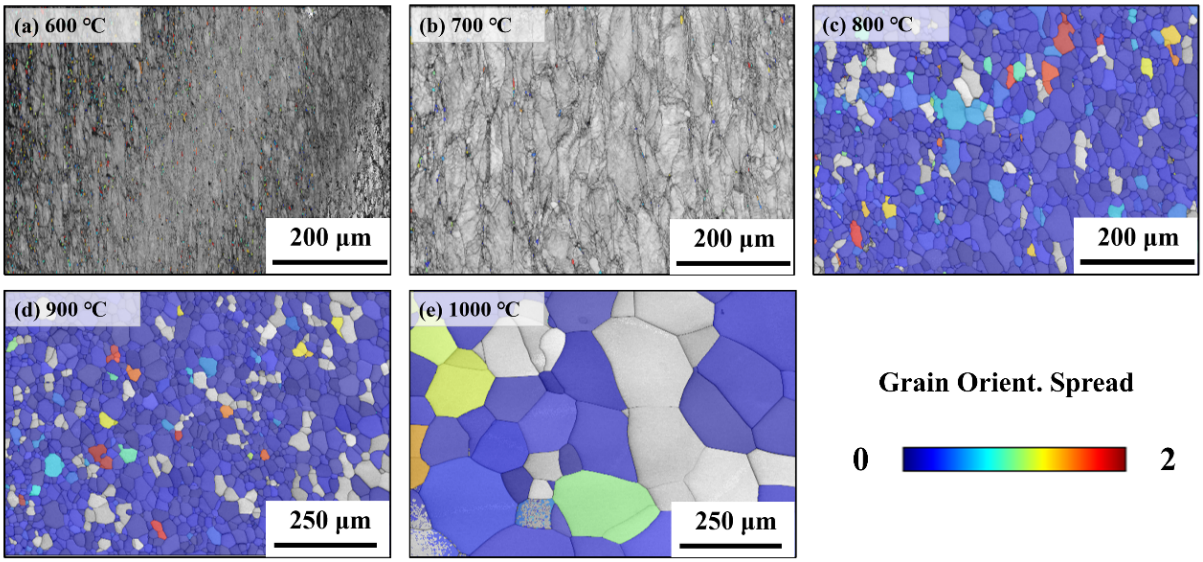


Figure 11. GOS distributions of vanadium wires after annealing at (**a**) 600 °C, (**b**) 700 °C, (**c**) 800 °C, (**d**) 900 °C, (**e**) 1000 °C. GOS threshold of 2° was used to differentiate recrystallized grains (colored) from deformed grains (gray).

3.2.2. Mechanical Properties at Different Annealing Temperatures

The tensile properties of vanadium wires after annealing at different temperatures are presented in Figure 13. The detailed tensile curves for each condition are provided in Supplementary Figure S3. As the annealing temperature increased, the strength decreased significantly, while the elongation first increased and then decreased. This behavior can be understood by considering the three annealing stages: recovery (600–700 °C), recrystallization (800–900 °C), and grain growth (1000 °C). At 600–700 °C, the material remained in the recovery stage. During recovery, dislocations undergo annihilation and rearrangement through glide and climb, and the internal residual stress is partially relieved, leading to a

gradual decrease in hardness and strength. However, the dense subgrain network and the high dislocation density introduced by cold drawing are largely retained; so, the elongation is only partially restored (17%), while the strength remains relatively high [31].

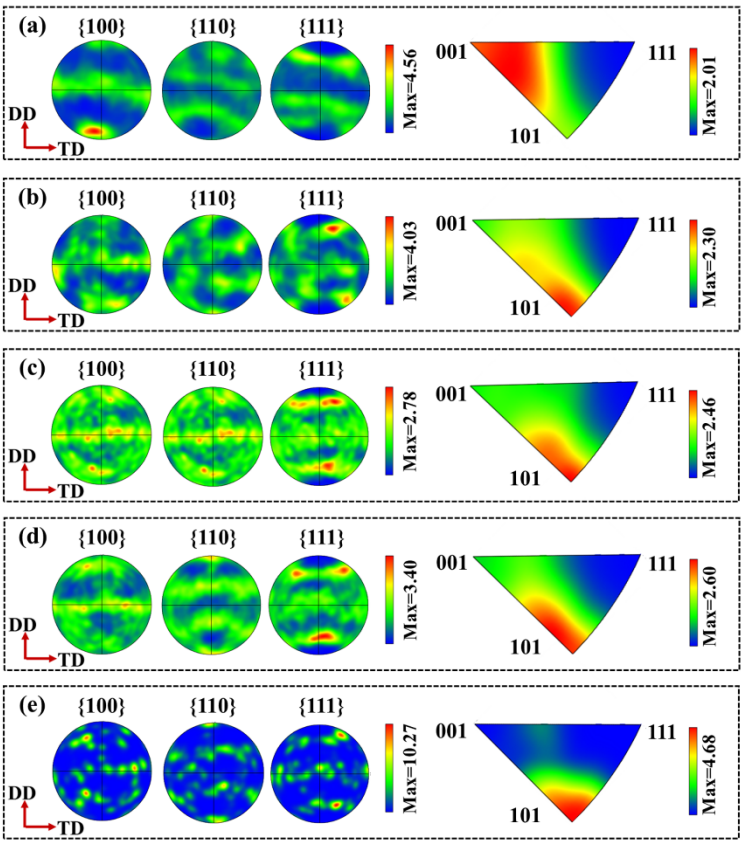


Figure 12. Pole figures and inverse pole figures of the vanadium wires at different annealing temperatures: (**a**) 600 °C; (**b**) 700 °C; (**c**) 800 °C; (**d**) 900 °C; (**e**) 1000 °C.

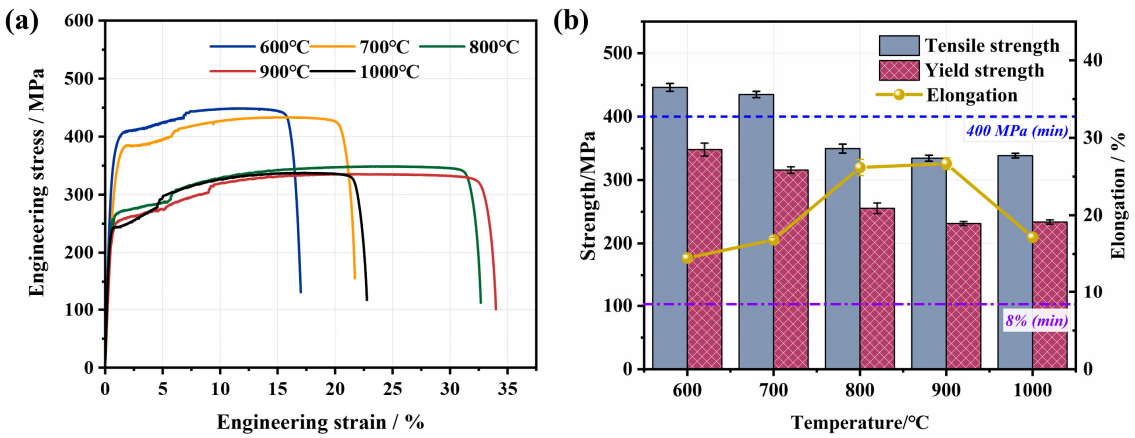


Figure 13. (**a**) Engineering stress–strain curves of vanadium wires at different annealing temperatures. (**b**) Tensile strength, yield strength, and elongation as functions of annealing temperatures. Each data point represents the average of at least three independent measurements under the same condition, and the error bars denote one standard deviation. The blue and purple dashed lines indicate the required minimum tensile strength (400 MPa) and elongation (8%), respectively.

When annealed at 800 °C, the tensile strength decreased to 349 MPa, and the elongation increased to 26.2%. This behavior is consistent with the microstructural evolution at this temperature, where recrystallization was completed and the microstructure transformed

from fibrous to equiaxed grains, and the work hardening was sufficiently eliminated. At 1000 °C, the elongation decreased sharply to 17.2%. This phenomenon can be attributed to significant grain growth, with the grain size reaching approximately 120.4 μm, which reduces the grain boundary area available for accommodating plastic deformation. This is consistent with the Hall–Petch relationship.

To analyze the effect of annealing temperature on microhardness, the hardness of wire cross-sections after annealing at different temperatures was measured, with the results shown in Figure 14. Compared with the as-drawn wire, the hardness of the annealed wires decreased overall. However, even after the completion of recrystallization, the phenomenon of higher hardness at the edge than at the center persisted. As grain growth proceeded, the hardness in the center gradually increased, leading to a progressive reduction in the hardness difference between the edge and the center. This indicates that the texture distribution across the wire cross-section becomes more uniform during annealing.

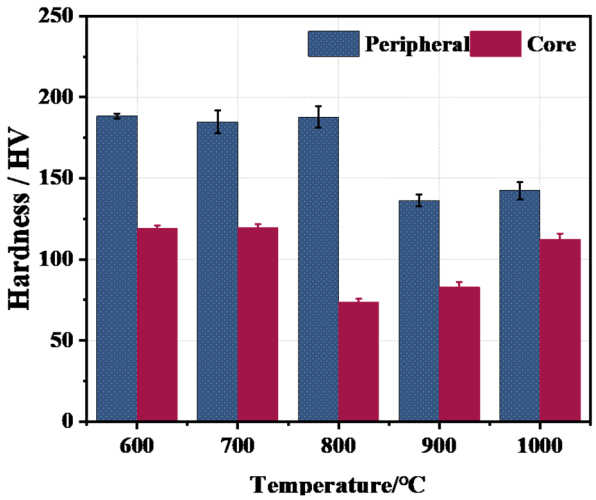


Figure 14. The microhardness at the peripheral and core regions of the vanadium wires at different temperatures. Each data point represents the average of at least three independent measurements under the same condition, and the error bars denote one standard deviation.

4. Discussion

4.1. Strengthening Mechanisms During Cold Drawing

It is well established that metallic strengthening mechanisms primarily include grain boundary strengthening (σ_{GB}), solid solution strengthening (σ_{SOL}), dislocation strengthening (σ_{DIS}), and precipitation strengthening (σ_{PRE}). In pure vanadium systems, solid solution strengthening and precipitation strengthening are negligible; thus, the yield strength can be expressed as [32–34]:

$$\sigma_{YS} = \sigma_0 + \sigma_{GB} + \sigma_{DIS} \quad (2)$$

where σ_0 is the intrinsic lattice frictional stress governing dislocation motion, measured at 96.8 MPa [35].

The Hall–Petch relation is often used to assess the contribution of grain boundaries to strength [36,37]:

$$\sigma_{GB} = K_y d^{-\frac{1}{2}} \quad (3)$$

where K_y is constant with the value of 209 MPa·μm1/2 [8], and d is the equivalent average grain size (as shown in Figure 15). In the present study, the average grain size measured on the longitudinal section decreased from 10.6 μm to 7.5 μm as the strain increased from 0 to 0.71. It should be noted, however, that the grains became significantly elongated along the drawing direction with increasing strain (Figure 3), which may introduce inaccuracies in

grain size quantification. To obtain a more accurate three-dimensional (3D) description of grain size, the transverse grain size and the equivalent average grain size were evaluated as functions of strain, as shown in Figure 16. Following the method described in Ref. [38], the grains were approximated as cylinders. The cylinder diameter was taken as the average transverse grain size (d_T) measured on the cross-section, and the corresponding cross-sectional EBSD maps are provided in Supplementary Figure S4. The cylinder length was taken as the average longitudinal grain size (L) measured along the drawing direction. The equivalent average grain size (d_{eq}) was then defined as the diameter of a sphere with the same volume as the cylinder:

$$d_{eq} = \left(\frac{3}{2} d_T^2 L\right)^{\frac{1}{3}} \quad (4)$$

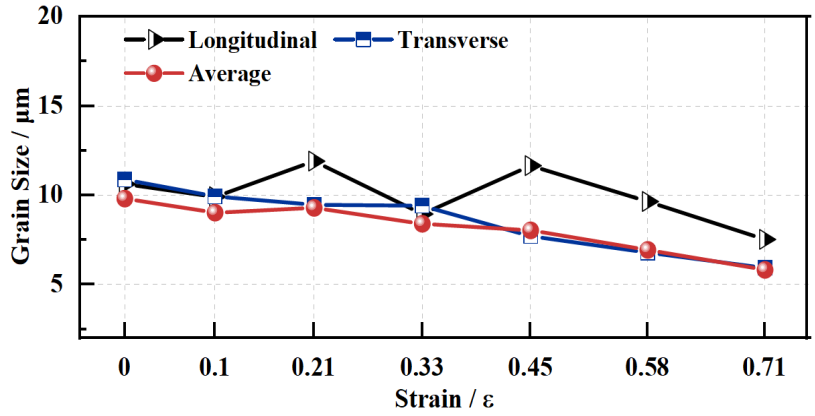


Figure 15. Longitudinal, transverse and equivalent average grain size of vanadium wires as functions of strain.

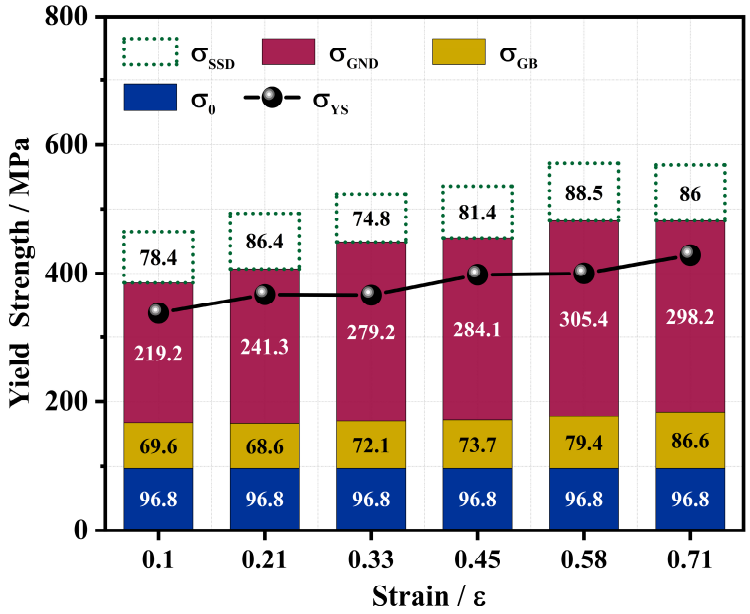


Figure 16. Contributions from lattice friction (σ_0), grain boundary strengthening (σ_{GB}), and dislocation strengthening ($\sigma_{DIS} = \sigma_{GND} + \sigma_{SSD}$) of the overall yield strength. The experimentally measured yield strength is denoted as σ_{YS}.

This definition accounts for the pronounced fibrous morphology of the grains after drawing and provides a more reliable 3D estimate of grain size than statistics obtained solely from longitudinal sections.

In the process of drawing vanadium wire, the dislocation density increases, significantly influencing the yield strength. The contribution of dislocation strengthening can be quantitatively analyzed using the Bailey–Hirsch equation [39–41]:

$$\sigma_{DIS} = M\alpha Gb(\rho_{tot})^{\frac{1}{2}} \tag{5}$$

where M is Taylor factor, α is a constant related to dislocation interactions; for polycrystalline bcc metals, M and α are 3.06 and 0.38, respectively [42–45]. G is shear modulus (46.7 GPa [46]), and b is Burgers vector (0.26 nm [46]). The total dislocation density (ρ_{tot}) comprises both GNDs and statistically stored dislocations (SSDs) [47]. The value of ρ_{tot} can be derived from Vickers microhardness (H_v) using a relationship based on the Taylor equation [40]:

$$\rho_{tot} = \frac{1}{13.5}\left(\frac{H_v - H_{v0}}{M}\gamma Gb\right)^2 \tag{6}$$

where $\gamma = 0.22$ is a constant, and H_{v0} is the microhardness of the initial, undeformed sample. However, the inherent hardness gradient across the wire diameter introduces uncertainty in selecting a representative value for $(H_v - H_{v0})$. To address this, the hardness is assumed to vary linearly from the center to the edge. Let R be the wire radius. H_C the hardness at the center, and H_P the hardness at the edge. The hardness at radius r is then given by

$$H(r) = H_C + (H_P - H_C)\frac{r}{R} 0 \le r \le R \tag{7}$$

The area-weighted average hardness is defined as:

$$\overline{H} = \frac{\int_0^R H(r)\cdot 2\pi r\, dr}{\int_0^R 2\pi r\, dr} \tag{8}$$

The calculated area-weighted average hardness $\overline{H}$ is then substituted into Equation (6) to determine ρ_{tot}, and the dislocation strengthening contribution σ_{DIS} is obtained from Equation (5).

The calculated contributions of individual strengthening mechanisms to the yield strength are summarized in Figure 16. It should be noted that the linear superposition of these contributions neglects both the interactions among different strengthening mechanisms and the influence of intrinsic defects. Consequently, the calculated sum systematically overestimates the experimental yield strength, especially at high strains. This discrepancy is attributed primarily to an overestimation of dislocation strengthening when the edge hardness is used, and, to a lesser extent, to the influence of intrinsic material defects. Dislocation strengthening (σ_{DIS}) was the dominant contributor across all strain levels. The contribution from geometrically necessary dislocations (σ_{GND}) increased substantially with strain, from 219.2 MPa at $\varepsilon = 0.1$ to 298.2 MPa at $\varepsilon = 0.71$. In contrast, grain boundary strengthening (σ_{GB}) provided a comparatively minor contribution, reaching only 86.6 MPa even at the highest strain of $\varepsilon = 0.71$, which is consistent with the limited grain refinement observed. Furthermore, the contribution from statistically stored dislocations (σ_{SSD}), represented by the dashed box in Figure 16, was significantly lower than that from GNDs. These results indicate the dominant role of GNDs in enhancing the yield strength of vanadium wires during cold drawing.

4.2. Microstructural Evolution and Processing Property Relationship

For vanadium wires for self-powered neutron detector, cold drawing is the critical process for strength enhancement. In this study, the microstructure evolution of vanadium wires during cold drawing is dominated by dislocation activities. Previous studies on

pure vanadium deformed by ECAP suggested that grain refinement was the dominant strengthening mechanism [6]. However, the present study focusing on the industrial cold drawing process revealed that dislocation strengthening is the dominant mechanism within the strain range up to ε = 0.71, indicating a significant difference in the strengthening mechanisms of pure vanadium under different deformation modes. At low strains, rapid dislocation multiplication leads to the formation of random dislocation tangles. Stress concentrations and crystallographic mismatches drive the preferential accumulation of GNDs near grain boundaries, forming dislocation walls that subdivide the original grains into subgrains. This is evidenced by a sharp increase in the LAGB fraction from 7.4% to 64.7% at ε = 0.33. Correspondingly, the ultimate tensile strength (UTS) increased rapidly to 419 MPa, while the elongation to failure decreased sharply to 5.9%, exhibiting a pronounced work hardening effect. With further straining, dislocation walls transform into sharper subgrain boundaries through dislocation absorption and recombination, increasing the LAGB fraction to 78.7% at ε = 0.58. At this stage, the UTS increased slowly to 458 MPa, the elongation to failure further decreased to 3.6%, and the subgrain structure became stable and uniformly distributed. Beyond this strain, the dislocation density tends to saturate and grain boundary migration becomes inhibited by the dense LAGB network (81.6% at ε = 0.71), leading to a deceleration in the LAGB growth rate [48,49]. The suppression of dynamic recovery enhances dislocation storage, thereby stabilizing the formed subgrain structure [50]. Consequently, the UTS increased only marginally to 467 MPa, and the elongation to failure remained at an extremely low level of 2.3%. Clearly, the elongation of the as-drawn wires is far below the requirement for vanadium wires. In addition, since SPNDs need to undergo long-term service at 400 °C, stabilization annealing of the vanadium wires is necessary to prevent signal drift caused by microstructural changes.

Generally, BCC refractory metal wires such as W, Mo, Nb, and Ta are subjected to recrystallization annealing after drawing to eliminate work hardening and restore ductility [51–54]. Some nuclear-grade materials, such as V–Cr–Ti alloys, are also solution-treated above the recrystallization temperature after rolling to obtain a uniform grain structure, aiming at high-temperature mechanical properties and irradiation stability after full recrystallization [55–57]. The annealing experiments conducted on the 1.4 mm high-purity vanadium wires over the temperature range of 600–1000 °C reveal three distinct microstructural evolution stages: recovery (600–700 °C), recrystallization (800–900 °C), and grain growth (1000 °C). After complete recrystallization, the elongation of the wires recovers to above 26%, but the tensile strength drops below 350 MPa. This significant strength reduction is attributed to the complete release of cold deformation stored energy, the drastic decrease in dislocation density, and the elimination of subgrain boundaries. The stored energy introduced by cold working provides the driving force for recrystallization, and its release during annealing leads to the removal of work hardening [58]. This strength level fails to meet the minimum requirement of 400 MPa for vanadium wires, indicating that complete recrystallization constitutes over-annealing for this application. In contrast, annealing at 600–700 °C results in a favorable balance of mechanical properties: the tensile strength remains above 430 MPa, while the elongation increases to more than 14%, as shown in Figure 13. During the recovery stage, dislocations undergo annihilation and rearrangement through slip and climb, and adjacent subgrains merge and coarsen, but no significant recrystallization nucleation occurs. This process partially relieves the internal stress and restores plasticity, while retaining most of the strengthening effects from cold deformation. Therefore, the process combination of high-strain cold drawing and recovery annealing can achieve the synergistic optimization of strength and plasticity for vanadium wires.

It should be noted that the long-term operating temperature of VSPNDs is 300–400 °C. This is significantly lower than the recovery annealing temperature used in this study and far below the recrystallization temperature. From a thermal activation perspective, purely thermal exposure at 300–400 °C has limited ability to drive recrystallization or rapid subgrain coarsening. Therefore, the recovered subgrain network is expected to remain thermally stable during service.

5. Conclusions

This study systematically investigates the microstructural evolution and changes in mechanical properties of high-purity vanadium wire during multi-pass cold drawing and vacuum annealing, aiming to establish an optimal processing window for vanadium wires used in self-powered neutron applications. The main conclusions are as follows:

1. Multi-pass cold drawing induces pronounced grain elongation and a fibrous microstructure in the vanadium wire. When the strain increases to 0.71, the average equivalent grain size decreases to 5.8 μm, while the geometrically necessary dislocation density rises to 4.68 $\times 10^{14}$ m^{-2}. The fraction of low-angle grain boundaries increases sharply to 81.6%, and the texture transforms from a dominant <110>//DD to <110>/<100> orientation.
2. Multi-pass cold drawing significantly strengthens the wire through work hardening. At ε = 0.71, the tensile strength increases from 328 MPa to 467 MPa, whereas the elongation drops to 2.3%. Dislocation strengthening is the dominant mechanism during cold drawing. Grain boundary strengthening makes a relatively small contribution due to limited grain refinement.
3. Annealing of the cold-drawn wire proceeds through three stages: recovery (600–700 °C), recrystallization (800–900 °C), and grain growth (1000 °C), with a critical recrystallization temperature of approximately 800 °C. Full recrystallization eliminates work hardening, resulting in a strength below the nuclear-grade requirement of 400 MPa.
4. The optimal processing route for vanadium wire is high-strain cold drawing followed by recovery annealing at 600–700 °C. This combination achieves a favorable strength–ductility balance, with a tensile strength exceeding 430 MPa and an elongation greater than 14%, meeting the specifications for detector applications.

Supplementary Materials: The following supporting information can be downloaded at: https://www.mdpi.com/article/10.3390/met16101137/s1, Figure S1: Photographs of the vanadium samples at different processing stages; Figure S2: Engineering stress–strain curves of vanadium wires at different drawing strains; Figure S3: Engineering stress–strain curves of vanadium wires at different annealing temperatures; Figure S4: Transverse-section EBSD analysis of vanadium wires at different drawing strains.

Author Contributions: Methodology, formal analysis, Investigation, Writing—original draft, Y.W. and S.P.; Funding acquisition, Resources, Supervision, Writing—review and editing, X.L.; Formal analysis, investigation, Data curation, R.T.; Funding acquisition, Resources, Supervision, Investigation, Project administration, Q.L.; Funding acquisition, Resources, Investigation, Project administration, A.Z.; Writing—original draft preparation, formal analysis, investigation, X.B.; Writing—review and editing, formal analysis, Supervision, Y.Z. All authors have read and agreed to the published version of the manuscript.

Funding: This research was funded by National Key R&D Program Project of China (NO. 2023YFB3210002) and the National Science and Technology Major Special Project of China (NO. 2017ZX06004004).

Data Availability Statement: The original contributions presented in this study are included in the article. Further inquiries can be directed to the corresponding author.

Conflicts of Interest: Yanhui Wang, Shilong Pan, Rui Tang, Qi Liu, Xinwei Bo and Yilong Zhong were employed by the Chongqing Material Research Institute Co., Ltd. Anzhong Zhao was employed by the Sinomach Academy of Science and Technology Co., Ltd. The remaining authors declare that the research was conducted in the absence of any commercial or financial relationships that could be construed as a potential conflict of interest.

References

1. Verma, V.; Barbot, L.; Filliatre, P.; Hellesen, C.; Jammes, C.; Svärd, S.J. Self-powered neutron detectors as in-core detectors for sodium-cooled fast reactors. *Nucl. Instrum. Methods Phys. Res. A* **2017**, *860*, 6–12. [CrossRef]
2. Khoshahval, F.; Park, M.; Shin, H.C.; Kim, Y. Vanadium, rhodium, silver and cobalt self-powered neutron detector calculations by RAST-K v2.0. *Ann. Nucl. Energy.* **2018**, *111*, 644–659. [CrossRef]
3. Wang, Y.H.; Liu, Q.; Zhang, A.Z. Progress in the development of key materials and components for self-powered neutron detector. *J. Funct. Mater.* **2020**, *51*, 10069.
4. Muroga, T. Vanadium for nuclear systems. *Compr. Nucl. Mater.* **2012**, *4*, 391–406. [CrossRef]
5. Zhang, J.; Han, W.Z. Oxygen solutes induced anomalous hardening, toughening and embrittlement in body-centered cubic vanadium. *Acta Mater.* **2020**, *196*, 122–132. [CrossRef]
6. Jiang, Z.Z.; Yu, S.H.; Chun, Y.B.; Shin, D.H. Grain refinement of pure vanadium by equal channel angular pressing. *Mater. Sci. Eng. A* **2008**, *479*, 285–292. [CrossRef]
7. Chun, Y.B.; Ahn, S.H.; Shin, D.H.; Watanabe, H. Combined effects of grain size and recrystallization on the tensile properties of cryorolled pure vanadium. *Mater. Sci. Eng. A* **2009**, *508*, 253–258. [CrossRef]
8. Hohenwarter, A.; Wurster, S. Deformation and fracture characteristics of ultrafine-grained vanadium. *Mater. Sci. Eng. A* **2016**, *650*, 492–496. [CrossRef]
9. Huang, Y.; Lemang, M.; Zhang, N.X.; Pereira, P.H.R.; Langdon, T.G. Achieving superior grain refinement and mechanical properties in vanadium through high-pressure torsion and subsequent short-term annealing. *Mater. Sci. Eng. A* **2016**, *655*, 60–69. [CrossRef]
10. Wang, Y.H.; Liu, Q.; Bo, X.W.; Wang, X.Y.; Jiang, C.D.; He, H.R. Research on sintering performance of high purity metal vanadium powders. *Powder Metall. Technol.* **2019**, *37*, 339–343, 349.
11. Kuwabara, T.; Kurishita, H.; Hasegawa, M. Microstructure control to improve mechanical properties of vanadium alloys for fusion applications. *J. Nucl. Mater.* **2000**, *283*, 611–615. [CrossRef]
12. Van Fossen, R.H.; Scott, T.E.; Carlson, O.N. The effect of strain rate and temperature on the ductility of pure and hydrogenated vanadium. *J. Less-Common Met.* **1965**, *9*, 437–451. [CrossRef]
13. Lindley, T.G.; Smallman, R.E. The plastic deformation of polycrystalline vanadium at low temperatures. *Acta Metall.* **1963**, *11*, 361–371. [CrossRef]
14. Behera, A.N.; Kapoor, R.; Sarkar, A. Hot deformation behavior of commercial pure vanadium. *Int. J. Refract. Met. Hard Mater.* **2024**, *122*, 106711. [CrossRef]
15. Lin, J.L.; Wang, G.S.; Zhang, X.F. Physical properties evolution of high-purity tantalum wire with the elongated grains caused by cold drawing. *Mater. Today Commun.* **2025**, *44*, 111983. [CrossRef]
16. Pantleon, W. Fiber textures revisited. *Mater. Charact.* **2025**, *223*, 114900. [CrossRef]
17. Cao, Y.; Ni, S.; Liao, X.; Zhu, Y. Structural evolutions of metallic materials processed by severe plastic deformation. *Mater. Sci. Eng. R* **2018**, *133*, 1–59. [CrossRef]
18. Baton, J.; Geslin, W.; Moussa, C. Orientation and deformation conditions dependence of dislocation substructures in cold deformed pure tantalum. *Mater. Charact.* **2021**, *171*, 110789. [CrossRef]
19. Yasunaga, K.; Iseki, M.; Kiritani, M. Dislocation structures introduced by high-speed deformation in bcc metals. *Mater. Sci. Eng. A* **2003**, *350*, 76–80. [CrossRef]
20. Wu, Z.; Li, Y.; Zhang, H.; Wang, T.; Zhang, C. Effect of drawing deformation on microstructure and mechanical properties of Fe-Cr-Co-W alloy. *Mater. Today Commun.* **2024**, *40*, 110214. [CrossRef]
21. Xie, D.; Liu, K.; Xian, X.; Ye, L.; Chen, Y. Effect of annealing temperature on the microstructure and properties of pure vanadium. *Rare Metal Mater. Eng.* **2008**, *37*, 1566–1569. [CrossRef]
22. Li, L.; Zhang, Z.; Zhang, P.; Zhang, P.; Zhang, Z.F. A review on the fatigue cracking of twin boundaries: Crystallographic orientation and stacking fault energy. *Prog. Mater. Sci.* **2023**, *131*, 101011. [CrossRef]
23. Fan, K.; Liu, B.; Yin, F.; He, J.; He, B.; Luo, Z. High-density low-angle grain boundaries enable exceptional combination of strength, ductility and toughness in 304 stainless steel. *J. Mater. Sci. Technol.* **2025**, *238*, 191–198. [CrossRef]
24. Ren, C.; Fang, Z.Z.; Xu, L.; Ligda, J.P.; Paramore, J.D.; Butler, B.G. An investigation of the microstructure and ductility of annealed cold-rolled tungsten. *Acta Mater.* **2019**, *162*, 202–213. [CrossRef]

25. Amodeo, R.J.; Ghoniem, N.M. A review of experimental observations and theoretical models of dislocation cells and subgrains. *Res. Mech.* **1988**, *23*, 137–160.
26. Purushottam Raj Purohit, R.R.P.; Arya, A.; Bojjawar, G.; Pelerin, M.; Van Petegem, S.; Proudhon, H.; Mukherjee, S.; Gerard, C.; Signor, L.; Mocuta, C.; et al. Revealing the role of microstructure architecture on strength and ductility of Ni microwires by in-situ synchrotron X-ray diffraction. *Sci. Rep.* **2019**, *9*, 79. [CrossRef] [PubMed]
27. Arya, A.; Suwas, S.; Gérard, C.; Signor, L.; Thilly, L.; Chokshi, A.H. Strength and microstructure evolution in nickel during large strain wire drawing. *Acta Mater.* **2021**, *221*, 117396. [CrossRef]
28. French, J.; Bai, X.M. Molecular dynamics studies of grain boundary mobility and anisotropy in BCC γ-uranium. *J. Nucl. Mater.* **2022**, *565*, 153744. [CrossRef]
29. Wu, D.; Zhu, Z.; Guo, S.; Luo, J.; Yan, X.; Wu, S.; Jiang, W.; Qiu, H.; Zhu, B.; He, J. Effect of annealing on microstructure of room-temperature unidirectional rolled EBM high-purity vanadium. *Mater. Charact.* **2026**, *234*, 116245. [CrossRef]
30. Park, Y.B.; Lee, D.N.; Gottstein, G. The evolution of recrystallization textures in body centred cubic metals. *Acta Mater.* **1998**, *46*, 3371–3379. [CrossRef]
31. Ogawa, Y.; Nagasaki, R. Recrystallization of V-20%Ti alloy. *J. Jpn. Inst. Met.* **1971**, *35*, 162–169. [CrossRef]
32. Fan, X.B.; Kang, X.; Zhang, Z.C.; Zhang, M.X.; Yuan, S.J. Influence of cryogenic deformation and post-deform aging on microstructure and mechanical properties of Al-Cu alloy. *J. Alloys Compd.* **2024**, *1005*, 175894. [CrossRef]
33. Kamikawa, N.; Sato, K.; Miyamoto, G.; Murayama, M.; Sekido, N.; Tsuzaki, K.; Furuhara, T. Stress-strain behavior of ferrite and bainite with nano-precipitation in low carbon steels. *Acta Mater.* **2015**, *83*, 383–396. [CrossRef]
34. Matsukawa, Y.; Yang, H.L.; Saito, K.; Murakami, Y.; Maruyama, T.; Iwai, T.; Murakami, K.; Shinohara, Y.; Kido, T.; Toyama, T.; et al. The effect of crystallographic mismatch on the obstacle strength of second phase precipitate particles in dispersion strengthening: Bcc Nb particles and nanometric Nb clusters embedded in hcp Zr. *Acta Mater.* **2016**, *102*, 323–332. [CrossRef]
35. Shen, J.; Nagasaka, T.; Tokitani, M.; Muroga, T.; Kasada, R.; Sakurai, S. Effects of titanium concentration on microstructure and mechanical properties of high-purity vanadium alloys. *Mater. Des.* **2022**, *224*, 111390. [CrossRef]
36. Petch, N.J. The cleavage strength of polycrystals. *J. Iron Steel Inst.* **1953**, *174*, 25–28.
37. Zhang, W.W.; Yang, Y.; Tan, Y.B.; Zeng, M.T.; Ma, M.; Xiang, S.; Zhao, F. Microstructure evolution and strengthening mechanisms of MP159 superalloy during room temperature rolling and cryorolling. *J. Alloys Compd.* **2022**, *908*, 164667. [CrossRef]
38. Zhou, B.; Wang, X.; Jiang, J.; Chen, C.; Zhang, X.; Niu, J.; Pei, J.; Huang, H.; Wang, D.; Yuan, G. Superior strength-ductility synergy of Mg-Nd-Zn-Zr alloy rod achieved by drawing at elevated temperatures. *Int. J. Plast.* **2024**, *175*, 103944. [CrossRef]
39. Bailey, J.E.; Hirsch, P.B. The dislocation distribution, flow stress, and stored energy in cold-worked polycrystalline silver. *Philos. Mag.* **1960**, *5*, 485–497. [CrossRef]
40. Taylor, G.I. The mechanism of plastic deformation of crystals. Part I. Theoretical. *Proc. R. Soc. Lond. A* **1934**, *145*, 362–387. [CrossRef]
41. Azzeddine, H.; Zavdoveev, A.; Brisset, F.; Motrunich, S.; Pashinska, O.; Thierry, B. EBSD analysis and mechanical properties of low-carbon steel during drawing with shear deformation. *Mater. Today Commun.* **2024**, *40*, 110100. [CrossRef]
42. Rice, P.M.; Zinkle, S.J. Temperature dependence of the radiation damage microstructure in V-4Cr-4Ti neutron irradiated to low dose. *J. Nucl. Mater.* **1998**, *258*, 1414–1419. [CrossRef]
43. Stoller, R.E.; Zinkle, S.J. On the relationship between uniaxial yield strength and resolved shear stress in polycrystalline materials. *J. Nucl. Mater.* **2000**, *283*, 349–352. [CrossRef]
44. Shen, J.J.; Li, Y.F.; Li, F. Microstructural characterization and strengthening mechanisms of a 12Cr-ODS steel. *Mater. Sci. Eng. A* **2016**, *673*, 624–632. [CrossRef]
45. Li, Q. Modeling the microstructure-mechanical property relationship for a 12Cr-2W-V-MoNi power plant steel. *Mater. Sci. Eng. A* **2003**, *361*, 385–391. [CrossRef]
46. Nagasaka, T.; Muroga, T.; Watanabe, H.; Yamasaki, K.; Heo, N.J.; Shinozaki, K.; Narui, M. Recovery of hardness, impact properties and microstructure of neutron-irradiated weld joint of a fusion candidate vanadium alloy. *Mater. Trans.* **2005**, *46*, 498–502. [CrossRef]
47. Ashby, M.F. The deformation of plastically non-homogeneous materials. *Philos. Mag.* **1970**, *21*, 399–424. [CrossRef]
48. Wang, X.; Xiao, Z.; Zhou, T.; Jiang, X. Deformation mechanism and properties evolution of a copper alloy with ultra-high strength after cold drawing and subsequent aging treatment. *Mater. Sci. Eng. A* **2024**, *912*, 146952. [CrossRef]
49. Liu, Q.; Fang, L.M.; Xiong, Z.W.; Yang, J.; Tan, Y.; Liu, Y.; Zhang, Y.J.; Tan, Q.; Hao, C.C.; Cao, L.H.; et al. The response of dislocations, low angle grain boundaries and high angle grain boundaries at high strain rates. *Mater. Sci. Eng. A* **2021**, *822*, 141704. [CrossRef]
50. Humphreys, F.J.; Hatherly, M. *Recrystallization and Related Annealing Phenomena*; Pergamon: Oxford, UK, 1995; p. 497.
51. Zhao, P.; Riesch, J.; Höschen, T.; Almanstötter, J.; Balden, M.; Coenen, J.W.; Himml, R.; Pantleon, W.; von Toussaint, U.; Neu, R. Microstructure, mechanical behaviour and fracture of pure tungsten wire after different heat treatments. *Int. J. Refract. Met. Hard Mater.* **2017**, *68*, 29–40. [CrossRef]

52. Yamanaka, M.; Shimada, K. Relation between tensile strength and annealing temperature for high purity niobium. *IEEE Trans. Appl. Supercond.* **2023**, *33*, 8401005. [CrossRef]
53. Zhu, J.; Deng, C.; Liu, Y.; Lin, N.; Liu, S. Effects of annealing temperature on recrystallization texture and microstructure uniformity of high purity tantalum. *Metals* **2019**, *9*, 75. [CrossRef]
54. Daw, J.; Rempe, J.; Knudson, D.; Crepeau, J.; Wilkins, S.C. *High Temperature Irradiation-Resistant Thermocouple Performance Improvements*; Idaho National Laboratory: Idaho Falls, ID, USA, 2009.
55. Chai, P.T.; Wang, Y.; Zhou, Y.Z.; Yang, X.S.; Li, J.F.; Liu, X.; Le, G.M.; Huang, X.F.; Yue, G.Z. Solution and aging behavior of precipitates in laser melting deposited V-5Cr-5Ti alloys. *J. Cent. South Univ.* **2021**, *28*, 1089–1099. [CrossRef]
56. Shen, J.; Saito, K.; Tokitani, M.; Muroga, T. Effects of annealing temperature on microstructure and hardness of cold rolled high-purity V-4Cr-xTi alloys. *Fusion Eng. Des.* **2023**, *194*, 113905. [CrossRef]
57. Chen, J.M.; Muroga, T.; Nagasaka, T.; Xu, Y.; Li, C.; Qiu, S.; Chen, Y. Precipitation behavior in V–6W–4Ti, V–4Ti and V–4Cr–4Ti alloys. *J. Nucl. Mater.* **2004**, *334*, 159–165. [CrossRef]
58. Alfonso, A. Thermal Stability of Warm-Rolled Tungsten. Ph.D. Thesis, DTU Mechanical Engineering, Kongens Lyngby, Denmark, 2015.

Disclaimer/Publisher's Note: The statements, opinions and data contained in all publications are solely those of the individual author(s) and contributor(s) and not of MDPI and/or the editor(s). MDPI and/or the editor(s) disclaim responsibility for any injury to people or property resulting from any ideas, methods, instructions or products referred to in the content.